ARTICLE

Stellar Bars in Isolated Gas-Rich Spiral Galaxies Do Not Slow Down

Angus Beane[1*], Lars Hernquist[1], Elena D'Onghia[2,3], Federico Marinacci[4], Charlie Conroy[1], Jia Qi[5], Laura V. Sales[6], Paul Torrey[5] and Mark Vogelsberger[7]

Elongated bar-like features are ubiquitous in galaxies, occurring at the centers of approximately two-thirds of spiral disks[1,2]. Due to gravitational interactions between the bar and the other components of galaxies, it is expected that angular momentum and matter will redistribute over long (Gyr) timescales in barred galaxies [3–5]. Previous work ignoring the gas phase of galaxies has conclusively demonstrated that bars should slow their rotation over time due to their interaction with dark matter halos [6–15]. We have performed a simulation of a Milky Way-like galactic disk hosting a strong bar which includes a state-of-the-art model of the interstellar medium and a live dark matter halo. In this simulation the bar pattern does not slow down over time, and instead remains at a stable, constant rate of rotation. This behavior has been observed in previous simulations using more simplified models for the interstellar gas but it has remained unexplained[16,17]. We propose that the gas phase of the disk and the dark matter halo act in concert to stabilize the bar pattern speed and prevent the bar from slowing down or speeding up. We find that in a Milky Way-like disk, a gas fraction of only about 5% is necessary for this mechanism to operate. This result naturally explains why nearly all observed bars rotate rapidly[18–20] and is especially relevant for our understanding of how the Milky Way arrived at its present state.

It has long been known that non-axisymmetric features in a stellar disk act to redistribute mass and angular momentum[3]. The interaction between a bar and a spheroid (either a dark matter halo or stellar bulge) has received considerable interest[4,5]. Stellar disks in isolation are prone to developing bars, [21] but the presence of a strong spherical potential (e.g., from a stellar bulge or dark matter halo) acts to stabilize the disk against bar formation[22,23]. Many numerical simulations have confirmed that a live dark matter halo generically exerts a negative torque on a bar, causing its pattern speed to decrease and its length and strength to increase[6–15]. Intuitively, the bar excites a wake of resonant material in a dark matter halo in a manner akin to dynamical friction. This wake lags the bar and thus exerts a negative torque on it. For a review of bar dynamics, see ref.[24]

The expectation that a dark matter halo acts to slow down a bar is in conflict with observational estimates of bar pattern speeds. Bar rotation rates are typically classified by the dimensionless ratio

$$\mathcal{R} = R_{\mathrm{CR}}/R_b, \tag{1}$$

where R_{CR} is the radius of corotation and R_b is the length of the bar.[†] Galaxies with $\mathcal{R} < 1.4$ are considered "fast rotators" while galaxies with $\mathcal{R} > 1.4$ are considered "slow rotators"[7]. Galaxies with $\mathcal{R} < 1$ are not thought to be stable[25]. Observational estimates of the pattern speeds of bars indicate that nearly all galaxies have $1 < \mathcal{R} < 1.4$[18–20,26].

The role of gas on the evolution of the bar is less well-understood. Since the gas phase typically only contributes about $10 - 20\%$ of the mass of a galaxy at the present day, one might naively expect it to have a subdominant effect on the bar. However, because gas is collisional, it can participate in non-resonant angular momentum exchange with the bar[27]. Thus, numerical work has shown that the gas phase can have a stronger influence on a bar than its contribution to the mass of a galaxy would suggest[17,28].

We have performed a simulation of a disk galaxy using the finite-volume gravito-hydrodynamics code AREPO[29]. In AREPO, the fluid is discretized as a moving Voronoi mesh. We use the additional physics in the galaxy formation module Stars and MUltiphase Gas in GaLaxiEs (SMUGGLE)[30]. SMUGGLE is a comprehensive and self-consistent galaxy formation model with a wide range of physical processes, including radiative heating/cooling, star formation, and stellar feedback. More detailed information on SMUGGLE is given in the Methods section. Our disk galaxy is a modified version of the GALAKOS model[31], which consists of a stellar disk, stellar bulge, and dark matter halo. After $\sim 2.5\,\mathrm{Gyr}$ of evolution, the GALAKOS disk forms a bar consistent with the Milky Way bar in terms of pattern speed and length ($\sim 40\,\mathrm{km/s/kpc}$[32] and $\sim 4.5\,\mathrm{kpc}$[33], respectively). We modify this setup to include a gas phase, the details of which are provided in the Methods section.

A mock stellar light image using filter profiles from the *Hubble Space Telescope* is shown in Fig. 1. The upper three panels show the disk in the N-body run while the lower three panels show the disk in the SMUGGLE run. Each column shows the disk $\sim 1\,\mathrm{Gyr}$ apart in time. There is a large qualitative difference in the evolution of the bar pattern between the two runs. We see that in the N-body case, the bar lengthens in time and grows in strength. In

[1] Center for Astrophysics | Harvard & Smithsonian, Cambridge, MA, USA.
[2] Department of Physics, University of Wisconsin-Madison, Madison, WI, USA.
[3] Department of Astronomy, University of Wisconsin-Madison, Madison, WI, USA.
[4] Department of Physics & Astronomy 'Augusto Righi', University of Bologna, Bologna, Italy.
[5] Department of Astronomy, University of Florida, Gainesville, FL, USA.
[6] Department of Physics & Astronomy, University of California, Riverside, CA, USA.
[7] Department of Physics, Massachusetts Institute of Technology, Cambridge, MA, USA.
* angus.beane@cfa.harvard.edu

[†]The radius of corotation R_{CR} is defined for circular orbits as the radius at which the orbital frequency is equal to the pattern speed, Ω_p, of a given non-axisymmetric feature. In a galaxy with a constant circular velocity V_c, it is given by $R_{\mathrm{CR}} = V_c/\Omega_p$.
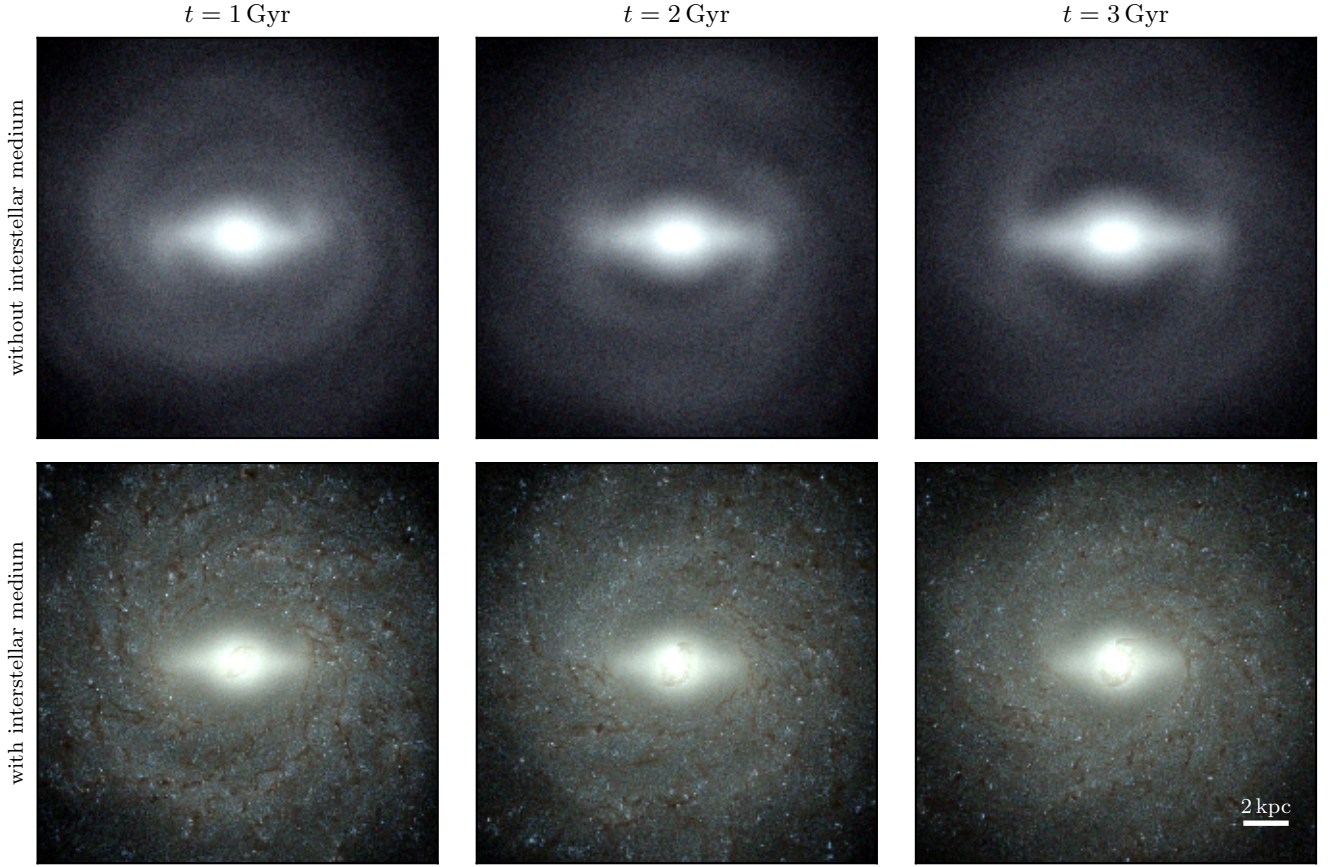
Figure 1 | Synthetic Hubble Space Telescope images of our simulations with and without the interstellar medium. The upper panels show an *N*-body only simulation while the lower panels show a simulation which includes the SMUGGLE model for the interstellar medium. Each panel is 20 kpc to a side. Columns show different points in time, separated by about 1 Gyr. We can see that in the *N*-body run, the bar grows in length and strength. In the SMUGGLE run, the bar remains at approximately the same length and strength over the course of the simulation. The *N*-body model is identical to the GALAKOS model, discussed in the text. Details on the production of these synthetic images is given in the Methods section.

the SMUGGLE case, the bar retains a similar length and strength between panels.

We show the time evolution of different bar properties in Fig. 2. In the upper panel, we show the pattern speed over time in the *N*-body (blue) and SMUGGLE (orange) runs. The pattern speed in the *N*-body case slows down while the pattern speed in the SMUGGLE case remains roughly constant. The slowing down of the pattern speed in the *N*-body case is consistent with a long line of numerical research on bars in *N*-body simulations[6-15]. However, in the SMUGGLE case the pattern speed remains constant. After the first Gyr of evolution, we find that the pattern speed increases by only $\sim$ 10% over the next 4 Gyr, compared to a $\sim$ 43% decrease in the pattern speed for the *N*-body run over the same interval. As we saw qualitatively in Fig. 1, the length of the bar in the *N*-body case grows over time while it remains roughly constant in the SMUGGLE case. This is also consistent with previous numerical work, which found that bars tend to grow as they slow down and the radius of corotation increases[7,10].

The bottom panel of Fig. 2 shows the torque exerted on the bar by different components. The solid lines indicate the torque on the bar by the dark matter halo, whereas the dashed line indicates the torque on the bar by the gas phase. In the *N*-body case, the halo exerts a steady negative torque on the bar, with an average torque from 1 to 4 Gyr of -58.0 in units of $10^{10} M_\odot$ (km/s)^2. The halo in the SMUGGLE case exerts a similar negative torque on the bar in the first Gyr of evolution, but after that the halo exerts a much smaller torque on the bar, averaging only -7.8 in the same units and over the same time interval. The gas in the SMUGGLE case exerts a steady positive torque averaging 11.7 over 1 Gyr in the same units.

The fact that the dark matter halo in the SMUGGLE case exerts a smaller negative torque on the bar can be understood in terms of the halo wake mechanism. In the *N*-body case, halo material which is resonant with the bar will form a wake which lags behind and exerts a negative torque on the bar, slowing it down[4-6].[‡] As the bar slows down, the location of the resonances in phase space changes, allowing halo material newly resonant with the bar to participate in forming the wake. However, the gas is a reliable source of positive torque on the bar, speeding the bar up. This stops the resonance location from changing such that the halo cannot reinforce the wake, arresting the process by which the halo can slow the bar down. We term this process "ex-

[‡]Since the bar is not a solid body, it is not guaranteed that a negative torque will slow it down - e.g. a negative torque could shred the bar, reducing its moment of inertia without changing its pattern speed. However, the bar seems to empirically respond to a negative torque induced by a halo wake by slowing down.
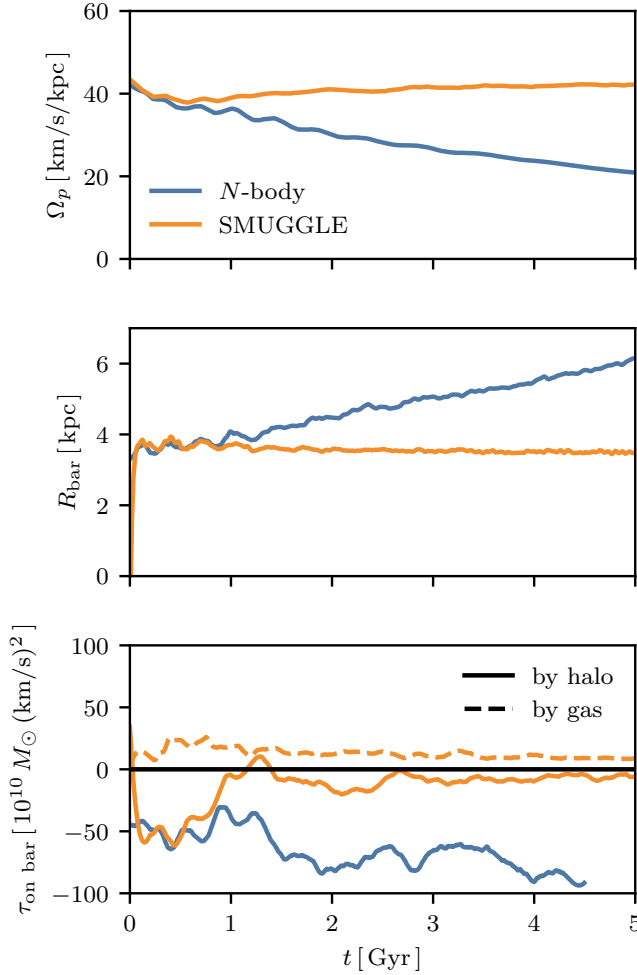
Figure 2 | Properties of the bar in our N-body and SMUGGLE simulations of a barred galaxy. The *upper panel* shows the evolution of the pattern speed. As expected, the bar in the N-body run slows down due to interactions between the bar and the dark matter halo. However, the bar in the SMUGGLE run does not slow down and instead remains at a constant pattern speed. The *middle panel* shows the evolution of the bar length. In the N-body case, the bar lengthens. This occurs because as the pattern speed drops, bar-like orbits at larger radii are possible. Stars are captured on these orbits, lengthening the bar. This process does not occur in the SMUGGLE cases since the bar pattern speed is not decreasing, and therefore the bar length remains constant. The *lower panel* shows the torque on the bar by different components. The solid lines show the torque exerted by the halo in both the N-body and SMUGGLE cases. The dashed line shows the torque exerted by the gas phase in the SMUGGLE run (there is no gas in the N-body run). Details on how these properties are calculated is given in the Methods section.

center and right panels of Fig. 3 show the halo wake with respect to the location of the bar in the N-body (center) and SMUGGLE (right) cases.

The presence of the gas can arrest the process by which additional material in the dark matter halo can contribute to a wake. However, this does not explain why the pattern speed in the SMUGGLE case is nearly constant over several Gyr. Naively, it would be a coincidence that the bar pattern speed remains constant in the SMUGGLE case, resulting from a chance cancellation of the halo and gas torques. However, a constant pattern speed in the presence of gas has been observed in a few simulations of barred galaxies with gas[16,17]. Previous work has argued this is due to the bar torquing gas inwards, but no explanation has been given for why it might remain constant.

We propose that an equilibrium mechanism is responsible for the pattern speed remaining approximately constant. In this scenario, residual negative torque from the dark matter halo balances out the positive torque from the gas phase. It has been shown when an analytic bar is forced to rotate at a constant pattern speed for a few Gyr, the halo exerts almost no torque on the bar[34]. We instead see over a several Gyr time span that the dark matter halo in our simulation is still able to support some negative torque.

We argue that the following occurs. First, the bar is not able to slow down quickly enough due to the positive torque of the infalling gas. This causes the resonant halo phase space at a particular pattern speed, $\Omega_{p,0}$, to become exhausted and no longer able to support a negative torque. Second, the gas is still exerting a positive torque on the bar, and therefore the pattern speed will again increase. Since at higher pattern speeds the halo has not yet been totally exhausted, the halo will once again be able to exert a negative torque on the bar. The pattern speed will then settle at a new value slightly higher than $\Omega_{p,0}$ where the gas and halo torques cancel. Over time, the pattern speed should slowly increase as the halo becomes progressively exhausted.

A clear prediction of this proposed mechanism is that the constant pattern speed a particular galaxy will end up is somewhat arbitrary. In the real universe for an isolated galaxy it would be the formation pattern speed of the bar while in our simulation it is the pattern speed of the bar when gas is added to the system. We tested this by adding gas to the system at a later time when the bar has further grown and slowed down with time. In our particular test, we added the gas at a time when the pattern speed is $\sim 30\,\mathrm{km/s/kpc}$. As shown in Fig. 4, we find that the pattern speed evolution is very similar between the two cases (orange and red lines). If anything, the system with a lower pattern speed seems to speed up more, which is consistent with our picture since the stronger bar should experience a larger torque from the gas as it is more efficient at driving gas inflows. We also show in the Methods that more slowly rotating bars at fixed bar strength are more efficient at driving gas inflows as well. Nonetheless, when the initial pattern speed is lower (red line), the addition of gas does not cause the pattern speed to quickly return to the higher value of our fiducial simulation (orange line).

We performed two additional tests to explore how our findings depend on the assumed model of the interstellar medium and the amount of gas present in the system. First, we performed a simulation of the same disk but with a simpler model of the interstellar medium[35], closer to standard methods used in cosmological simulations of galaxy formation. We find that the pattern speed evolution is nearly the same in this case, and so conclude that our result is not sensitive to the details of the model for the interstellar medium. The details of this experiment are given in

haustion."

We can test this interpretation by measuring the angle offset between the halo wake and the bar. If the wake and the bar are aligned (i.e., there is no angle offset), then the wake cannot exert a negative torque on the bar. This angle is plotted in the left panel of Fig. 3, which shows that the angle offset is larger in the N-body case than in the SMUGGLE case by about a factor of two. The
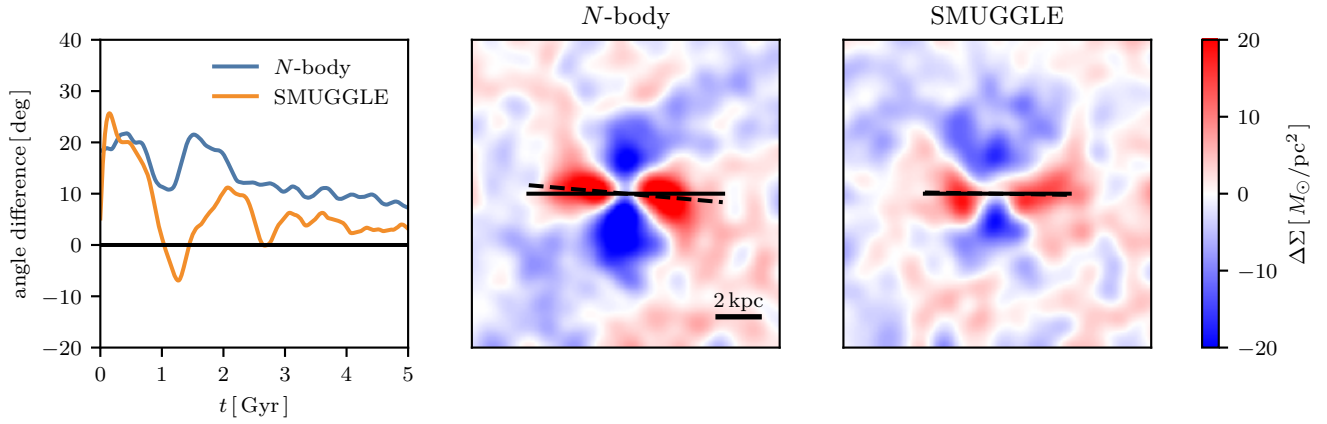
Figure 3 | The wake excited in the dark matter halo. The dark matter halo wake is shown in the N-body case (*middle panel*) and SMUGGLE case (*right panel*) after 2.6 Gyr of evolution. The *middle* and *right panels* show a surface density projection in the x-y plane of the dark matter halo after an axisymmetric average has been subtracted. The solid line indicates the direction of the bar while the dashed line indicates the direction of the halo wake (both measured by taking the second Fourier component within a sphere of all material within a radius of 4 kpc). The *left panel* shows the time evolution of the angle difference between the bar and the halo wake, as measured from the second Fourier component. After the first Gyr, the angle difference in the SMUGGLE case is smaller than in the N-body case by about a factor of two, reflecting how the dark matter halo in the SMUGGLE case is unable to exert as negative a torque on the bar as in the N-body case.
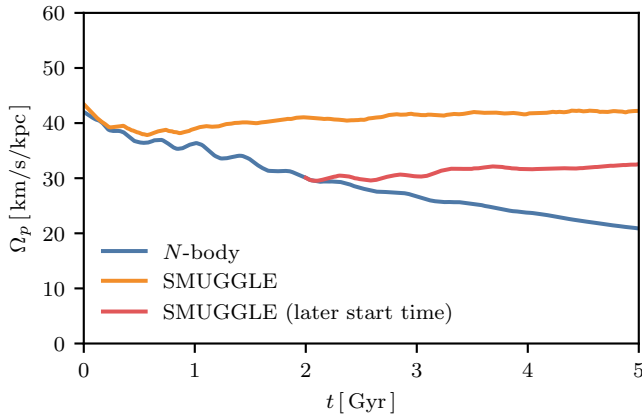
Figure 4 | Pattern speed evolution with a lower initial pattern speed. We tested the evolution of our system when gas is added to the N-body run at a later time, but with all other simulation parameters kept the same. The setup is therefore identical to our previous runs just with a bar that is larger, stronger, and with a lower pattern speed. We find that the pattern speed evolution is very similar to our fiducial case, except that the bar retains its original pattern speed. This indicates a mechanism which keeps the bar at its formation pattern speed, and that there is not a particular pattern speed which the system tends to.

the Methods section.

Second, we performed a set of simulations in which we decreased the initial gas mass of the disk. We essentially find for our disk, our proposed mechanism operates as long as the gas contributes about 5% of the total mass of the disk. If the gas available is below this threshold, then the pattern speed will decrease in a similar fashion to standard N-body simulations. Importantly, arbitrarily increasing the gas fraction does not cause the pattern speed to continuously increase. This is consistent with our proposed equilibrium mechanism and with previous studies of barred galaxies with varying gas fractions.[17] The exact critical gas fraction above which our mechanism operates is likely dependent on the properties of the bar, disk, and dark matter halo – further work is needed to characterize how this gas fraction varies with such properties. Details on this test in which we varied the gas mass of the disk are given in the Methods section.

We note that ref.[26] found that the rotation parameter $\mathcal{R}$ positively correlates with gas fraction, such that galaxies with higher gas fractions are rotating more slowly. However, it is not obvious this is in tension with our result since the gas fraction of galaxies correlates with other galactic properties[36]. Furthermore, the measurement of pattern speeds is a delicate process still prone to large error bars.

The implications of our findings are numerous. First, we naturally explain why nearly all observed galaxies are fast rotators without requiring the inner regions of dark matter halos to be underdense[7,37] or requiring new physics[38,39]. Second, we show that the role of gas is of paramount importance in studies which attempt to uncover the nature of dark matter from its effect of slowing down the bar[40,41]. Third, we provide an explanation for how the Milky Way's bar could be both long-lived and a fast rotator, of which there is some observational evidence[42]. And finally, we complicate the picture of radial mixing expected to sculpt the Milky Way's disk [43,44], a process which relies upon the pattern speed of the bar to change with time (though our work does not alter expectations for radial mixing induced by spiral arms[45]).

Barred galaxies in cosmological simulations of galaxy formation continue to be in conflict with observations by producing bars which rotate too slowly[46–48]. However, the pattern speeds of bars in both cosmological simulations and the real universe can be affected by environmental processes not included in our simulation – e.g., satellite infall[49], non-sphericity[28] or rotation[50–53] in the dark matter halo, or perhaps even the gaseous circumgalactic medium. Naturally, extending our present work to account for such effects is a crucial next step in understanding the formation and evolution of galactic bars.

We found that below a certain gas fraction, bars should still be able to slow down. Therefore, we expect barred spiral galaxies which have been gas-poor for extended periods of time to be rotating very slowly. We therefore predict that observations which target such galaxies (e.g., lenticular barred galaxies[36]) would find slowly rotating bars. There does exist one example of a galaxy which is known to be a slow rotator – the low surface brightness galaxy UGC 628[54]. This galaxy has been studied in detail by ref.[55], who note that it indeed has a low gas fraction for galaxies of its type. We predict a general trend that bars in gas-rich spiral galaxies should rotate quickly while bars in gas-poor spiral galaxies should rotate slowly.

1. Eskridge, P. B. *et al.* The Frequency of Barred Spiral Galaxies in the Near-Infrared. AJ **119**, 536–544 (2000). astro-ph/9910479.
2. Menéndez-Delmestre, K., Sheth, K., Schinnerer, E., Jarrett, T. H. & Scoville, N. Z. A Near-Infrared Study of 2MASS Bars in Local Galaxies: An Anchor for High-Redshift Studies. ApJ **657**, 790–804 (2007). astro-ph/0611540.
3. Lynden-Bell, D. & Kalnajs, A. J. On the generating mechanism of spiral structure. MNRAS **157**, 1 (1972).
4. Tremaine, S. & Weinberg, M. D. Dynamical friction in spherical systems. MNRAS **209**, 729–757 (1984).
5. Weinberg, M. D. Evolution of barred galaxies by dynamical friction. MNRAS **213**, 451–471 (1985).
6. Hernquist, L. & Weinberg, M. D. Bar-Spheroid Interaction in Galaxies. ApJ **400**, 80 (1992).
7. Debattista, V. P. & Sellwood, J. A. Constraints from Dynamical Friction on the Dark Matter Content of Barred Galaxies. ApJ **543**, 704–721 (2000). astro-ph/0006275.
8. Athanassoula, E. & Misiriotis, A. Morphology, photometry and kinematics of N-body bars - I. Three models with different halo central concentrations. MNRAS **330**, 35–52 (2002). astro-ph/0111449.
9. Athanassoula, E. Bar-Halo Interaction and Bar Growth. ApJ **569**, L83–L86 (2002). astro-ph/0203368.
10. Athanassoula, E. What determines the strength and the slowdown rate of bars? MNRAS **341**, 1179–1198 (2003). astro-ph/0302519.
11. O'Neill, J. K. & Dubinski, J. Detailed comparison of the structures and kinematics of simulated and observed barred galaxies. MNRAS **346**, 251–264 (2003). astro-ph/0305169.
12. Holley-Bockelmann, K., Weinberg, M. & Katz, N. Bar-induced evolution of dark matter cusps. MNRAS **363**, 991–1007 (2005). astro-ph/0306374.
13. Martinez-Valpuesta, I., Shlosman, I. & Heller, C. Evolution of Stellar Bars in Live Axisymmetric Halos: Recurrent Buckling and Secular Growth. ApJ **637**, 214–226 (2006). astro-ph/0507219.
14. Weinberg, M. D. & Katz, N. The bar-halo interaction - II. Secular evolution and the religion of N-body simulations. MNRAS **375**, 460–476 (2007). astro-ph/0601138.
15. Dubinski, J., Berentzen, I. & Shlosman, I. Anatomy of the Bar Instability in Cuspy Dark Matter Halos. ApJ **697**, 293–310 (2009). 0810.4925.
16. Friedli, D. & Benz, W. Secular evolution of isolated barred galaxies. I. Gravitational coupling between stellar bars and interstellar medium. A&A **268**, 65–85 (1993).
17. Villa-Vargas, J., Shlosman, I. & Heller, C. Dark Matter Halos and Evolution of Bars in Disk Galaxies: Varying Gas Fraction and Gas Spatial Resolution. ApJ **719**, 1470–1480 (2010). 1004.4899.
18. Corsini, E. M. Direct measurements of bar pattern speeds. *Memorie della Societa Astronomica Italiana Supplementi* **18**, 23 (2011). 1002.1245.
19. Aguerri, J. A. L. *et al.* Bar pattern speeds in CALIFA galaxies. I. Fast bars across the Hubble sequence. A&A **576**, A102 (2015). 1501.05498.
20. Guo, R. *et al.* SDSS-IV MaNGA: pattern speeds of barred galaxies. MNRAS **482**, 1733–1756 (2019). 1810.03257.
21. Hohl, F. Numerical Experiments with a Disk of Stars. ApJ **168**, 343 (1971).
22. Ostriker, J. P. & Peebles, P. J. E. A Numerical Study of the Stability of Flattened Galaxies: or, can Cold Galaxies Survive? ApJ **186**, 467–480 (1973).
23. Hohl, F. Suppression of bar instability by a massive halo. AJ **81**, 30–36 (1976).
24. Sellwood, J. A. & Wilkinson, A. Dynamics of barred galaxies. *Reports on Progress in Physics* **56**, 173–256 (1993). astro-ph/0608665.
25. Contopoulos, G. How far do bars extend. A&A **81**, 198–209 (1980).
26. Garma-Oehmichen, L. *et al.* SDSS-IV MaNGA: bar pattern speed estimates with the Tremaine-Weinberg method and their error sources. MNRAS **491**, 3655–3671 (2020). 1911.00090.
27. Hopkins, P. F. & Quataert, E. An analytic model of angular momentum transport by gravitational torques: from galaxies to massive black holes. MNRAS **415**, 1027–1050 (2011). 1007.2647.
28. Athanassoula, E., Machado, R. E. G. & Rodionov, S. A. Bar formation and evolution in disc galaxies with gas and a triaxial halo: morphology, bar strength and halo properties. MNRAS **429**, 1949–1969 (2013). 1211.6754.
29. Springel, V. E pur si muove: Galilean-invariant cosmological hydrodynamical simulations on a moving mesh. MNRAS **401**, 791–851 (2010). 0901.4107.
30. Marinacci, F., Sales, L. V., Vogelsberger, M., Torrey, P. & Springel, V. Simulating the interstellar medium and stellar feedback on a moving mesh: implementation and isolated galaxies. MNRAS **489**, 4233–4260 (2019). 1905.08806.
31. D'Onghia, E. & L. Aguerri, J. A. Trojans in the Solar Neighborhood. ApJ **890**, 117 (2020). 1907.08484.
32. Gaia Collaboration *et al.* Gaia Data Release 3: Mapping the asymmetric disc of the Milky Way. *arXiv e-prints* arXiv:2206.06207 (2022). 2206.06207.
33. Wegg, C., Gerhard, O. & Portail, M. The structure of the Milky Way's bar outside the bulge. MNRAS **450**, 4050–4069 (2015). 1504.01401.
34. Chiba, R. & Schönrich, R. Oscillating dynamical friction on galactic bars by trapped dark matter. MNRAS **513**, 768–787 (2022). 2109.10910.
35. Springel, V. & Hernquist, L. Cosmological smoothed particle hydrodynamics simulations: a hybrid multiphase model for star formation. MNRAS **339**, 289–311 (2003). astro-ph/0206393.
36. Blanton, M. R. & Moustakas, J. Physical Properties and Environments of Nearby Galaxies. ARA&A **47**, 159–210 (2009). 0908.3017.
37. Debattista, V. P. & Sellwood, J. A. Dynamical Friction and the Distribution of Dark Matter in Barred Galaxies. ApJ **493**, L5–L8 (1998). astro-ph/9710039.
38. Roshan, M. *et al.* Barred spiral galaxies in modified gravity theories. MNRAS **503**, 2833–2860 (2021). 2103.01794.
39. Roshan, M. *et al.* Fast galaxy bars continue to challenge standard cosmology. MNRAS **508**, 926–939 (2021). 2106.10304.
40. Chiba, R., Friske, J. K. S. & Schönrich, R. Resonance sweeping by a decelerating Galactic bar. MNRAS **500**, 4710–4729 (2021). 1912.04304.
41. Chiba, R. & Schönrich, R. Tree-ring structure of Galactic bar resonance. MNRAS **505**, 2412–2426 (2021). 2102.08388.
42. Bovy, J. *et al.* Life in the fast lane: a direct view of the dynamics, formation, and evolution of the Milky Way's bar. MNRAS **490**, 4740–4747 (2019). 1905.11404.
43. Bird, J. C., Kazantzidis, S. & Weinberg, D. H. Radial mixing in galactic discs: the effects of disc structure and satellite bombardment. MNRAS **420**, 913–925 (2012). 1104.0933.
44. Hayden, M. R. *et al.* Chemical Cartography with APOGEE: Metallicity Distribution Functions and the Chemical Structure of the Milky Way Disk. ApJ **808**, 132 (2015). 1503.02110.
45. Sellwood, J. A. & Binney, J. J. Radial mixing in galactic discs. MNRAS **336**, 785–796 (2002). astro-ph/0203510.
46. Algorry, D. G. *et al.* Barred galaxies in the EAGLE cosmological hydrodynamical simulation. MNRAS **469**, 1054–1064 (2017). 1609.05909.
47. Peschken, N. & Łokas, E. L. Tidally induced bars in Illustris galaxies. MNRAS **483**, 2721–2735 (2019). 1804.06241.
48. Fragkoudi, F. *et al.* Revisiting the tension between fast bars and the ΛCDM paradigm. A&A **650**, L16 (2021). 2011.13942.
49. Purcell, C. W., Bullock, J. S., Tollerud, E. J., Rocha, M. & Chakrabarti, S. The Sagittarius impact as an architect of spirality and outer rings in the Milky Way. Nature **477**, 301–303 (2011). 1109.2918.
50. Saha, K. & Naab, T. Spinning dark matter haloes promote bar formation. MNRAS **434**, 1287–1299 (2013). 1304.1667.
51. Long, S., Shlosman, I. & Heller, C. Secular Damping of Stellar Bars in Spinning Dark Matter Halos. ApJ **783**, L18 (2014). 1402.1491.
52. Collier, A., Shlosman, I. & Heller, C. What makes the family of barred disc galaxies so rich: damping stellar bars in spinning haloes. MNRAS **476**, 1331–1344 (2018). 1712.02802.
53. Collier, A., Shlosman, I. & Heller, C. Dark matter bars in spinning haloes. MNRAS **488**, 5788–5801 (2019). 1811.00033.
54. Chemin, L. & Hernandez, O. A slow bar in a dark matter dominated galaxy. A&A **499**, L25–L28 (2009). 0904.3442.
55. Chequers, M. H., Spekkens, K., Widrow, L. M. & Gilhuly, C. Simulating a slow bar in the low surface brightness galaxy UGC 628. MNRAS **463**, 1751–1758 (2016). 1608.08248.

56. Springel, V., Di Matteo, T. & Hernquist, L. Modelling feedback from stars and black holes in galaxy mergers. MNRAS **361**, 776–794 (2005). astro-ph/0411108.

57. Hernquist, L. An Analytical Model for Spherical Galaxies and Bulges. ApJ **356**, 359 (1990).

58. Eilers, A.-C., Hogg, D. W., Rix, H.-W. & Ness, M. K. The Circular Velocity Curve of the Milky Way from 5 to 25 kpc. ApJ **871**, 120 (2019). 1810.09466.

59. Vasiliev, E. AGAMA: action-based galaxy modelling architecture. MNRAS **482**, 1525–1544 (2019). 1802.08239.

60. Kalberla, P. M. W. & Dedes, L. Global properties of the H I distribution in the outer Milky Way. Planar and extra-planar gas. A&A **487**, 951–963 (2008). 0804.4831.

61. Evans, N. J., Kim, J.-G. & Ostriker, E. C. Slow Star Formation in the Milky Way: Theory Meets Observations. ApJ **929**, L18 (2022). 2204.02314.

62. Miville-Deschênes, M.-A., Murray, N. & Lee, E. J. Physical Properties of Molecular Clouds for the Entire Milky Way Disk. ApJ **834**, 57 (2017). 1610.05918.

63. Grand, R. J. J. *et al.* The Auriga Project: the properties and formation mechanisms of disc galaxies across cosmic time. MNRAS **467**, 179–207 (2017). 1610.01159.

64. Chabrier, G. Galactic Stellar and Substellar Initial Mass Function. PASP **115**, 763–795 (2003). astro-ph/0304382.

65. Hopkins, P. F. *et al.* FIRE-2 simulations: physics versus numerics in galaxy formation. MNRAS **480**, 800–863 (2018). 1702.06148.

66. Petersen, M. S., Weinberg, M. D. & Katz, N. Dark matter trapping by stellar bars: the shadow bar. MNRAS **463**, 1952–1967 (2016). 1602.04826.

67. Hernquist, L. & Katz, N. TREESPH: A Unification of SPH with the Hierarchical Tree Method. ApJS **70**, 419 (1989).

68. Camps, P. & Baes, M. SKIRT 9: Redesigning an advanced dust radiative transfer code to allow kinematics, line transfer and polarization by aligned dust grains. *Astronomy and Computing* **31**, 100381 (2020). 2003.00721.

69. Bruzual, G. & Charlot, S. Stellar population synthesis at the resolution of 2003. MNRAS **344**, 1000–1028 (2003). astro-ph/0309134.

70. Jones, A. P., Köhler, M., Ysard, N., Bocchio, M. & Verstraete, L. The global dust modelling framework THEMIS. A&A **602**, A46 (2017). 1703.00775.

71. Lupton, R. *et al.* Preparing Red-Green-Blue Images from CCD Data. PASP **116**, 133–137 (2004). astro-ph/0312483.

72. Rodrigo, C., Solano, E. & Bayo, A. SVO Filter Profile Service Version 1.0. IVOA Working Draft 15 October 2012 (2012).

73. Rodrigo, C. & Solano, E. The SVO Filter Profile Service. In *XIV.0 Scientific Meeting (virtual) of the Spanish Astronomical Society*, 182 (2020).

74. Savitzky, A. & Golay, M. J. E. Smoothing and differentiation of data by simplified least squares procedures. *Analytical Chemistry* **36**, 1627–1639 (1964).

Data Availability Simulation output at a selection of timesteps as well as the initial conditions will be made publicly available. Simulation output at higher timestep frequency will be available upon request.

Code Availability A public version of the AREPO code is available at https://arepo-code.org/. An associated GitHub repository containing analysis and plotting scripts will be made publicly available (currently private). For the submission stage, we have included a tarball of this repository (associated file gasbar.tar.gz).

Supplementary Information Supplementary information is available for this manuscript.

METHODS

Initial setup

The initial setup of the galactic disk used in this work follows closely the GALAKOS model[31], which uses a modified version of the `MakeNewDisk` code[56]. The GALAKOS model has three components - a radially exponential and vertically isothermal stellar disk, and a stellar bulge and dark matter halo following a Hernquist profile[57]. All N-body runs in this work used the same setup parameters as the GALAKOS disk, more details of which can be found in the original paper.

The addition of the gas phase was done as follows. The version of `MakeNewDisk` used for the original GALAKOS model can generate a gas disk which is radially exponential and in vertical gravito-hydrodynamic balance. We modified the radial profile of this code in order to allow us to generate a disk with a constant surface density within some cut-off radius, and then exponentially declining beyond that radius with the scale-length of the stellar disk. Our fiducial model used an initial surface density of $20\,M_\odot/\mathrm{pc}^2$ and a cut-off radius of $9.3\,\mathrm{kpc}$. The initial gas disk is generated with a temperature of $10^4\,\mathrm{K}$ and solar metallicity.

After generating the gaseous disk in this way, we stitched the gas disk together with the GALAKOS N-body disk (and bulge and dark matter halo) after the GALAKOS disk has been allowed to evolve for $1.5\,\mathrm{Gyr}$. The purpose of allowing the GALAKOS disk to evolve first for a short period of time is to allow for the bar to form unimpacted by the presence of the gas (which would normally disrupt the formation of the bar). Throughout this work, we consider $t = 0$ for the N-body run to be the time at which we added the gas phase for the SMUGGLE run (i.e. we ignore the first $1.5\,\mathrm{Gyr}$ of evolution of the N-body disk when the bar is forming). We made one additional modification when stitching the gas disk together with the N-body disk - we created a hole within the central $4\,\mathrm{kpc}$. This hole guards against an initial dramatic infall of gas within the bar region, which we found to destroy the bar. It is not uncommon for observed barred galaxies to have gas deficits in the bar region (though not in the very center)[24], and so our practice of allowing the gas distribution to have a hole in the central region is consistent with our choice to begin the simulations with a bar already formed.

Our setup is initially out of equilibrium, but we found that after $\sim 500\,\mathrm{Myr}$, the entire system has settled into a steady-state configuration and initial transients appear not to affect the results after this point. The constant surface density of the initial gas disk is important for ensuring the gas disk is dense enough in order for comparisons to real galaxies to be appropriate.

We computed the circular velocity curve of our model using the `AGAMA` package[59]. We fit the baryonic component (stellar disk, bulge, gas, and newly formed stars) with an axisymmetric cylindrical spline with 20 grid points in both the radial and vertical direction spanning 0.2 to $50\,\mathrm{kpc}$ in the radial direction and from 0.02 to $10\,\mathrm{kpc}$ in the vertical direction. We fit the dark matter halo using a spherically symmetric multipole fit with a maximum angular harmonic coefficient of $l = 2$. We plot the circular velocity curve in Extended Data Fig. 1 compared to observational estimates[58]. The SMUGGLE disk (which includes additional mass in the form of gas) has a slightly higher circular velocity than the N-body disk which, itself, is slightly higher than the observational estimates.

We also show the evolution of the surface density profile in Extended Data Fig. 5 We find that in our simulation the atomic and molecular gas surface density and the SFR surface density is broadly consistent with the expected values for the Milky
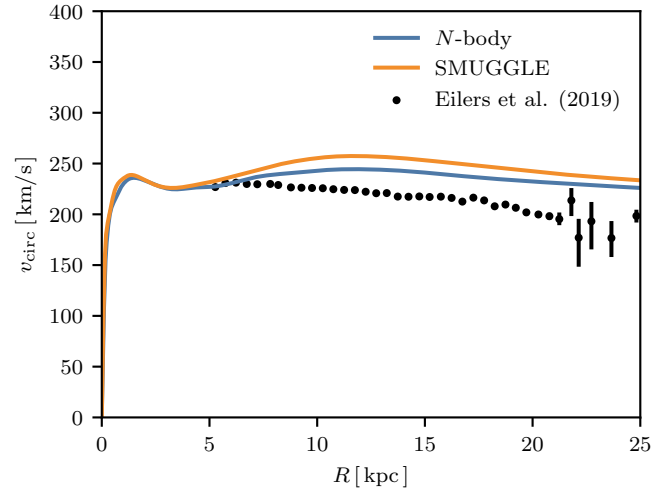
Extended Data Figure 1 | The circular velocity curve of our initial setups. This curve is shown for the N-body run (blue) and the SMUGGLE run (orange) compared to observational estimates for the Milky Way[58]. We see that the circular velocity curve for both runs is marginally larger than the Milky Way's, but still comparable. The SMUGGLE circular velocity curve is larger than the N-body curve due to the additional mass in the gas phase.

Way[60,61]. The discrepancy between 1 and $4\,\mathrm{kpc}$ in the molecular and SFR surface density is likely due to the fact that the distances to molecular clouds which underlines this work used a simple kinematic distance based on an axisymmetric model of the Milky Way[62], which is not accurate in the bar region where gas has large non-circular velocities.

We used a mass resolution of $7.5 \times 10^3\,M_\odot$ for the baryonic components (initial stellar disk, stellar bulge, and gas) and a mass resolution of $3.75 \times 10^4\,M_\odot$ for the dark matter halo. This mass resolution is closest to "level 3" in the AURIGA simulations[63]. This corresponds to approximately 6.4×10^6 particles in the stellar disk, 1.1×10^6 in the bulge, 1.2×10^6 in the gas disk, and 25.3×10^6 in the dark matter halo. We used a softening length of $0.02\,\mathrm{kpc}$ for all components. Snapshots were saved at equal intervals of 0.005 in the time units of the simulation ($\mathrm{kpc}/(\mathrm{km/s}) \sim 1\,\mathrm{Gyr}$).

SMUGGLE model

We use the Stars and MUltiphase Gas in GaLaxiEs (SMUGGLE) model[30] implemented within the moving-mesh, finite-volume hydrodynamics and gravity code AREPO[29]. The SMUGGLE model additionally includes radiative heating and cooling, star formation, and stellar feedback. Explicit gas cooling and heating of the multi-phase interstellar medium is implemented, covering temperature ranges between 10 and $10^8\,\mathrm{K}$.

Star formation occurs in cells above a density threshold ($n_{\mathrm{th}} = 100\,\mathrm{cm}^{-3}$) with a star-formation efficiency of $\epsilon = 0.01$. Star formation converts gas cells into star particles which represent single stellar populations with a Chabrier initial mass function[64]. For each star particle, the deposition of energy, momentum, mass, and metals from stellar winds and supernovae is modeled. Photo-ionization and radiation pressure are modeled using an approximate treatment. A more detailed description of this model can be found in the flagship SMUGGLE paper[30].
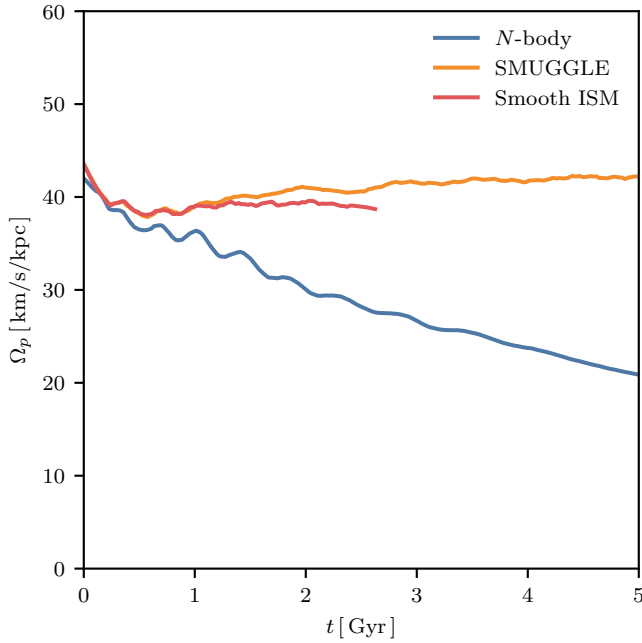
Extended Data Figure 2 | Pattern speed evolution of a smooth ISM model. This evolution is shown for the fiducial disk in the N-body (blue), SMUGGLE (orange), and smooth ISM (red) cases. The smooth ISM model is an older model for the ISM which treats its multiphase nature in a subgrid fashion[35]. This fundamentally differs from the SMUGGLE model, which explicitly resolve the hot and cold phases of the ISM[30]. The pattern speed in the smooth ISM case is broadly similar to the evolution in the SMUGGLE case. This shows that the stability of the pattern speed is not simply a result of our assumed model for the ISM.
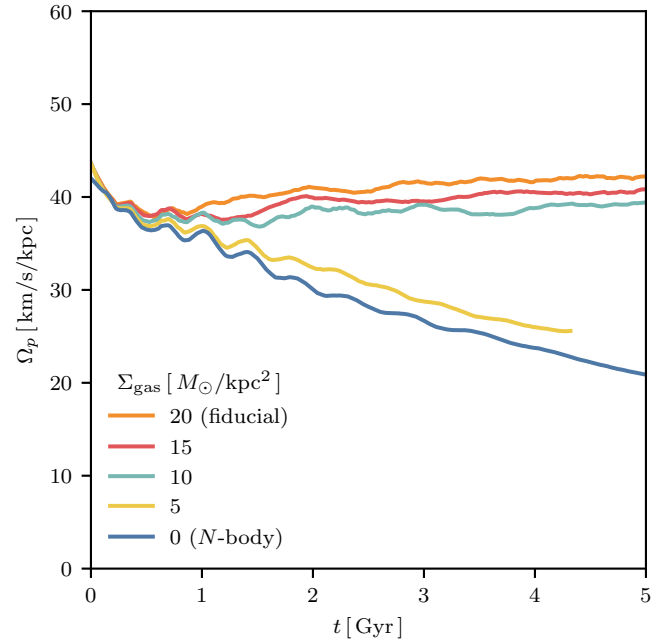
Extended Data Figure 3 | Pattern speed evolution with varying gas fractions. We explored the impact of lowering the initial gas surface density of our fiducial disk on the evolution of the pattern speed. The surface densities we tested of 20, 15, 10, and $5\,M_\odot/\mathrm{kpc}^2$ correspond to initial gas fractions of 16%, 10%, 7%, and 4%. We find that initial surface densities 20, 15, and $10\,M_\odot/\mathrm{kpc}^2$ result in bars which remain at a constant pattern speed, while an initial surface density of $5\,M_\odot/\mathrm{kpc}^2$ results in a bar which slows down in roughly the same manner as the N-body case.

We used the fiducial model parameters, except that we increased the number of effective neighbors N_{ngb} for the deposition of feedback from 64 to 512. We found that a lower value of N_{ngb} resulted in inefficient photo-ionization feedback since the photoionizing budget had not been exhausted after deposition into 64 neighboring cells. We also used an updated version of SMUGGLE using a new mechanical feedback routine similar to the one described in ref.[65] This updated routine is a tensor renormalization which ensures linear and angular momentum conservation to machine precision.

Smooth interstellar medium model

In addition to the SMUGGLE model, we considered a simpler model of the interstellar medium based upon ref.[35] In this model, the multiphase nature of the interstellar medium is modeled in a subgrid manner by allowing each resolution element to have a "cold" and "hot" component, with the equation of state of the gas suitably modified. Gas is allowed to interchange between the "cold" and "hot" components through processes such as cooling and stellar feedback. Cold gas is allowed to undergo star formation. The pattern speed evolution of this setup is given in Extended Data Fig. 2, which shows that the pattern speed evolves in a similar manner to the SMUGGLE case shown in Fig. 2.

Varying gas fraction

We also performed a test in which we varied the initial gas frac-

tion of the disk. In our fiducial run, we set the surface density of the gas disk from $4\,\mathrm{kpc}$ to $\sim 9.3\,\mathrm{kpc}$ to be $20\,M_\odot/\mathrm{pc}^2$. We also ran with surface densities of 15, 10, and $5\,M_\odot/\mathrm{pc}^2$. These correspond to initial gas fractions of approximately 16%, 10%, 7%, and 4%. The pattern speed evolution is shown in Extended Data Fig. 3 We find that the bar in disks with initial surface densities of 20, 15, and $10\,M_\odot/\mathrm{pc}^2$ evolve with a constant pattern speed while the bar in a disk with initial surface density of $5\,M_\odot/\mathrm{kpc}^2$ slows down at a similar rate to the N-body case.

As a result, we conclude that for the disk, bar, and halo properties considered in this work, a gas fraction of only approximately 5% is necessary in order for the proposed stabilizing mechanism to operate.

Varying pattern speed

When the bar slows down, we argue that this induces a larger positive torque from the gas phase. Only gas within corotation will flow inwards, while gas outside corotation will flow outwards[27]. Since the corotation radius is larger for more slowly rotating bars, it follows that more slowly rotating bars should be more efficient at driving gas inflows and thus experience a larger positive torque from the gas phase.

We performed an experiment to test this hypothesis by forcing the stellar disk in the SMUGGLE run to rotate at a constant angular rate and measuring the torque on the bar by the gas phase at different rotation rates. The result of this experiment is illustrated in Extended Data Fig. 4, which shows that a more
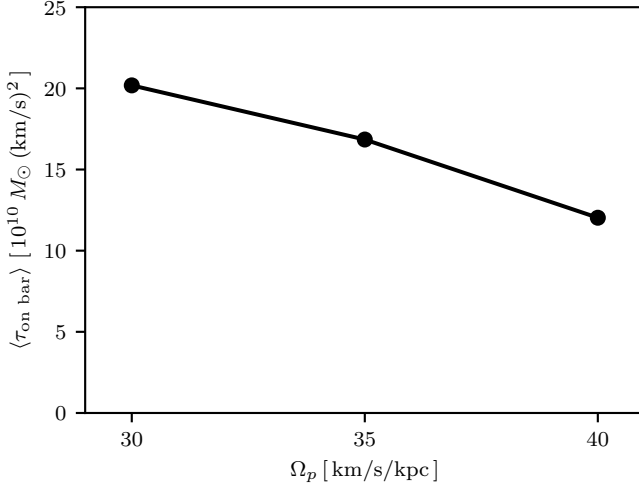
Extended Data Figure 4 | Average torque exerted by gas on a bar which rotates at a fixed pattern speed. Since only gas within the corotation radius is able to infall and slower bars have larger corotation radii, slower bars experience a larger net torque than faster bars. The setup of the simulations used here is identical to the SMUGGLE case discussed earlier and in the Methods section, except the N-body disk is rotated as a solid body with a constant angular velocity.

slowly rotating bar experiences a larger positive torque from the
624 gas.

625 **Bar analysis**
626 The analysis of various bar properties is performed as follows.
627 First, the pattern speed is measured from the angle of the second
628 Fourier component. We measured the second Fourier compo-
629 nent by computing,

$$A_2 = \sum_i m_i e^{i2\phi_i}$$
$$A_0 = \sum_i m_i, \tag{2}$$

630 where m_i and ϕ_i are the mass and azimuthal angle of each par-
631 ticle, respectively. We computed A_2 and A_0 in cylindrical bins
632 of width 0.5 kpc from radii of 0 to 30 kpc. We defined the angle
633 of the bar ϕ_b to be twice the angle of the complex number A_2 as
634 measured in the bin extending from a radius of 2.5 to 3 kpc. Af-
635 ter correcting for the periodicity of ϕ_b, we measured the pattern
636 speed as one-half the two-sided finite gradient of ϕ_b as a function
637 of time.

638   The time evolution of the bar strength, defined as the maxi-
639 mum of $|A_2/A_0|$ as a function of radius, is shown in Extended
640 Data Fig. 6. The quantity $|A_2/A_0|$ varies from 0 to 1, with
641 larger values indicating a stronger bar pattern. We see that in
642 the N-body case, $|A_2/A_0|$ increases over time as the bar pat-
643 tern slows. This is consistent with previous N-body simulations
644 which showed a clear correlation between the bar pattern speed
645 and the bar strength[10]. In the SMUGGLE case, we see that the bar
646 strength has an initial drop but then remains at a roughly con-
647 stant, but slightly decreasing, strength. This is consistent with
648 the pattern speed in the SMUGGLE case being roughly constant
649 or slightly increasing.

650   Computing the length of the bar and the torque on the bar by
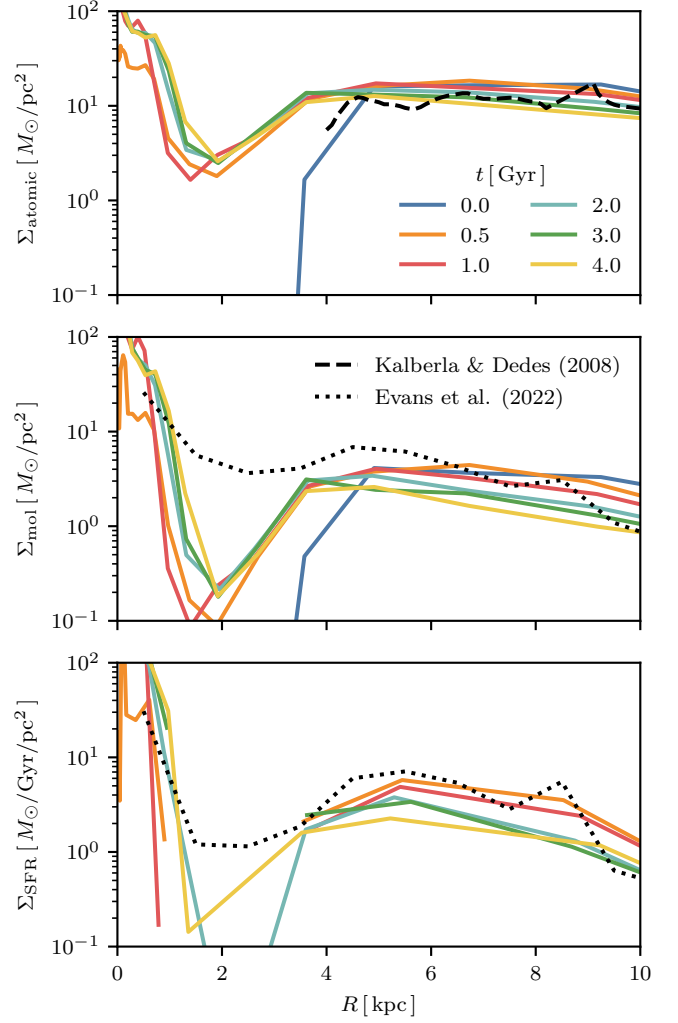
Extended Data Figure 5 | Evolution of gas and SFR surface density profiles. The time evolution of the atomic gas surface density (*upper*), molecular gas surface density (*middle*) and the star formation rate (SFR) surface density (*lower*) at various times during our fiducial simulation. Colored lines indicate the profiles at selected times during the simulation while the black dashed lines indicate observations for the atomic gas[60] and black dotted lines indicate a model which allows the CO-to-H_2 conversion factor X_{CO} to vary with metallicity[61]. Molecular gas surface densities were provided separately (N. Evans, private communication). We see that the molecular gas and SFR surface densities are within an order of magnitude of the Milky Way's typical values at all times. We see a sharp decrease in the gas and SFR surface densities along the extent of the bar from ~ 1 to ~ 4 kpc, related to the gas inflow in this region.

different components requires us to decompose the disk into a
component which is trapped by the bar and a component which 652
is untrapped. In order to do this, we follow closely the technique 653
developed in ref.[66] We analyzed the orbit of each star particle 654
(meaning initial disk, bulge, and newly formed stars) by extract- 655
ing the x-y positions of the apoapse of each in a frame corotating 656
with the bar (apoapses are defined as local maxima in r). For 657
each apoapse, we searched for the 19 closest apoapses in time and 658
applied a k-means clustering algorithm on this set of 20 points 659
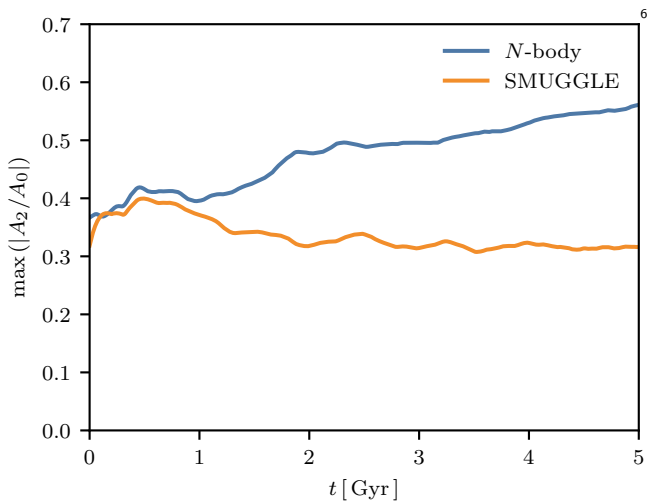
Extended Data Figure 6 | Evolution of bar strength. The bar strength is measured as the maximum of the second Fourier component divided by the zeroth Fourier component. We see that in the N-body case (blue) the bar strength increases with time, consistent with previous results showing that the bar strength increases as bars slow down. In the SMUGGLE case (orange), we see that the bar strength remains roughly constant, possibly slightly decreasing with time. This is also consistent with the expected relation between pattern speed and strength since the bar in this case is not slowing down.

with $k = 2$. We then computed for each of the two clusters the average angle from the bar $\langle\Delta\phi\rangle_{0,1}$, the standard deviation in R of the points $\sigma_{R0,1}$, and the average radius of the cluster $\langle R\rangle_{0,1}$. At each apoapse, a particle was considered to be in the bar if it met the following criteria:

$$\max\left(\langle\Delta\phi\rangle_{0,1}\right) < \pi/8 \qquad (3)$$

$$\frac{\sigma_{R0} + \sigma_{R1}}{\langle R\rangle_0 + \langle R\rangle_1} < 0.22 \qquad (4)$$

These criterion are slightly different and simplified from the ones used in ref.[66], but we found them to empirically work well at decomposing the disk into a bar and disk component. In Extended Data Fig. 7, we show an example of this decomposition. The *left* panel shows a surface density projection of the stellar disk and bulge (including newly formed stars) from the SMUGGLE model after 1 Gyr of evolution in a frame such that the bar is aligned with the x-axis. The *middle* panel shows a projection of the subset of stars that are identified as being trapped in the bar and the *right* panel shows a projection of the stars that are not identified as being trapped. The fact that the *right* panel is roughly axisymmetric indicates the bar decomposition is performing adequately.

After the disk has been decomposed into a trapped and untrapped component, we measured the bar length as being the radius R_b which encapsulates 99% of the stars identified as being trapped in the bar, allowing for some outliers. For the computation of the torque, we used the tree algorithm in `MakeNewDisk`[56] customized to be accessible from `Python` using `Cython`. This algorithm is based on the `TREESPH` code[67]. We constructed a tree with an opening angle of 0.35 using only the star particles identified as being trapped in the bar. We then queried the tree at the locations of all resolution elements in the other components and computed the torque of the bar on such components. The torque on the bar by the other components is simply the negative of the torque on the other components by the bar. A similar method was applied in measuring the torque for the disk when the pattern speed is kept constant, as is done in Fig. 4.

Idealized mock light images
We created synthetic mock light images at 1024^2 resolution in Fig. 1 for the *Hubble Space Telescope* using a post-processed Monte Carlo radiation transfer simulation with the SKIRT9 code including secondary emission from dust[68]. Emission from star particles was calculated assuming a Bruzual-Charlot spectral energy distribution[69] and a Chabrier initial stellar mass function[64]. The luminosity from each star particle was smoothed using a cubic spline kernel with each star particle being assigned a smoothing length equal to its distance to its 32nd closest neighbor. We launched 10^9 photon packets per simulation segment. For star particles which were present in the initial simulation (i.e., initial disk and bulge particles), we assumed that they have an age of 5 Gyr and solar metallicity. For star particles in the SMUGGLE simulation which are newly formed, we used their recorded ages and metallicities.

For the SMUGGLE simulations, we included absorption and emission from dust. We assumed the THEMIS (The Heterogeneous dust Evolution Model for Interstellar Solids) dust model[70] to convert gas metallicity and mass density to dust mass density. For the N-body simulations we ran the SKIRT9 code in a mode without an obscuring medium, but otherwise applied the same procedure.

We used the profiles for filters F814W, F606W, and F475W on the Advanced Camera for Surveys (ACS) instrument for red, green, and blue pixel values, respectively. Filtered fluxes were converted to RGB values using an arcsinh scaling following ref.[71]. Scalings and cutoff values were adjusted manually to create visually appealing images. Filter profiles were provided by the Spanish Virtual Observatory Filter Service[72,73].

Plotting details
We saved snapshots in intervals of 0.005 in the time units of the simulation, kpc/(km/s), which is very nearly equal to 1 Gyr (it is ~ 0.977 Gyr). Therefore, throughout this work we referred to the native code time unit as Gyr. None of our results are sensitive to this choice.

In order to remove numerical noise in several quantities we computed, we applied a Savitzky-Golay filter[74] as implemented in `scipy` using a window length of 81 and polynomial order of 3. This filter was applied to plots of pattern speeds, bar lengths and strengths, torques, and angle differences.

total disk　　　　　　　barred disk　　　　　　　unbarred disk
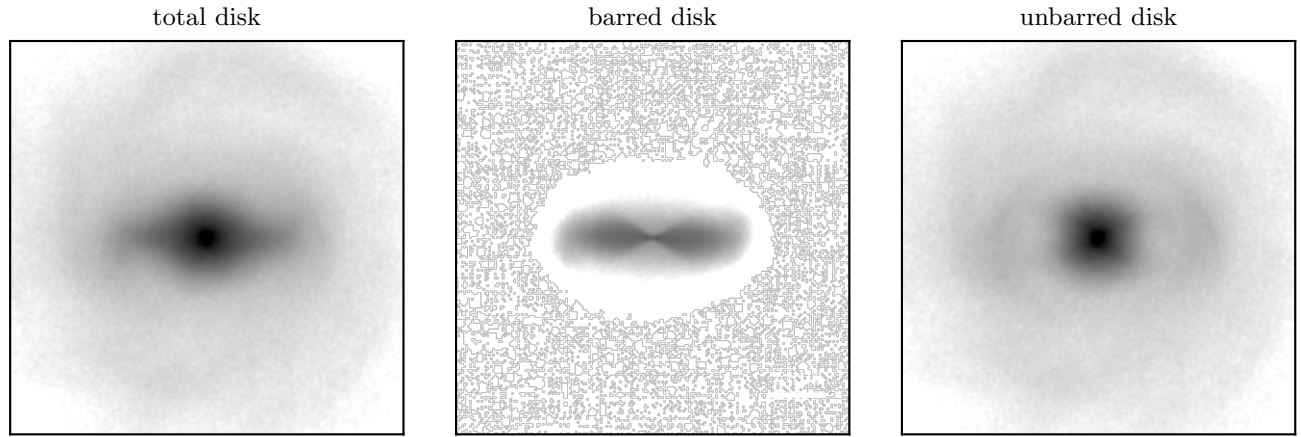
Extended Data Figure 7 | Disk decomposition into the barred and unbarred disk. This procedure is based on ref.[66] The *left panel* shows a face-on surface density projection through the stellar component of the SMUGGLE simulation (disk and bulge) at $t = 1\,\mathrm{Gyr}$. The *middle panel* shows the component of the disk identified as being trapped in the bar while the *right panel* shows the component of the disk identified as not being trapped in the bar. The fact that the untrapped stars form a roughly axisymmetric structure indicates our bar decomposition is sufficiently accurate.